AMERICAN
METEOROLOGICAL
SOCIETY

Journal of Climate

The DOI for this manuscript is doi: 10.1175/2010JCLI3851.1

Modeling of Regional Hydroclimate Change over the Indian Subcontinent: Impact of the Expanding Thar Desert

Massimo Bollasina and Sumant Nigam

Department of Atmospheric and Oceanic Science

University of Maryland, College Park, MD

Submitted to *Journal of Climate* on May 14, 2010, revised on November 16, 2010.

Corresponding author:

Massimo Bollasina
Department of Atmospheric and Oceanic Science
3417 Computer and Space Science Building
University of Maryland, College Park, MD 20742-2425
E-mail: massimo@atmos.umd.edu

ABSTRACT

The Thar Desert between northwestern India and Pakistan is the most densely populated desert region in the world and vast surrounding areas are affected by rapid soil degradation and vegetation loss. The impact of an expanded desert (implemented by changing vegetation type and related greenness fraction, albedo, surface roughness length, emissivity, etc.) on the South Asian summer monsoon hydroclimate is investigated by means of 7-month 4-member ensemble sensitivity experiments with the Weather Research and Forecasting model.

It is found that extended desertification significantly affects the monsoon at local and large-scale. Locally, the atmospheric water cycle weakens, since precipitation, evaporation, and atmospheric moisture convergence all decrease; soil moisture and runoff reduce too. Air temperature cools due to albedo increase (the desert makes the area brighter) and reduction of surface turbulent fluxes; the cooling is partially offset by adiabatic descent generated to maintain thermodynamic balance and originating at the northern flank of the low-level anticyclone forced by desert subsidence. Regionally, an anomalous northwesterly flow over the Indo-Gangetic Plain weakens the monsoon circulation over northeastern India, causing precipitation to decrease and the formation of an anomalous anticyclone in the region. As a result, the middle Troposphere cools due to decreased latent-heat release but the ground heats up due to cloudiness reduction. At larger scale, interaction between the anomalous circulation and the mountains leads to precipitation increase over the Eastern Himalayas and Indochina.

The findings of this study reveal that the expansion of the Thar Desert can lead to a pronounced and large-scale impact on summer monsoon hydroclimate, with a potential to redistribute precious water over South Asia.

1. Introduction

The Thar (or Great Indian) Desert is located between northwestern India and Pakistan. It receives an average annual precipitation between 150 and 450 mm (from west to east), 90% of which occurs during summer (Sikka 1997; Chauhan 2003). In summer the Thar Desert is the center of the most intense surface low-pressure system in the global tropics. Several crops are cultivated in the area surrounding the Thar Desert, with major harvesting in winter or early spring (when maximum greenness is observed), benefitting from previous year monsoon precipitation (e.g., USDA 1994; see also Fig. 1). The Thar Desert itself appears darker on global albedo maps compared to other deserts (e.g., the Sahara), given the presence of dry open grassland vegetation (Rahmani and Soni 1997). To the west, the Desert is bounded by the Indus River and its relatively green valley from which many irrigation canals depart. The Thar Desert territory is the most densely populated desert region in the world and vast areas of northwestern India are affected by rapid soil degradation and vegetation loss (e.g., Ravi and Huxman 2009). Maps of soil moisture regions show a drastic westward expansion of the "arid" regime in recent years (Singh et al. 2005). Niyogi et al. (2010) showed monsoon precipitation over northwestern India to have a strong negative trend in the last decades, providing evidence for the role of anthropogenic land-use modifications (i.e., agricultural intensification) in causing the observed rainfall pattern[1]. As a result of population growth and extensive agricultural practices, groundwater over northwestern India is being progressively depleted (Rodell et

[1] A relationship between increased irrigation, vegetation development, and July surface temperature and rainfall over the whole Indian Subcontinent is suggested also by Lee et al. (2009).

al. 2009). The region is under the threat of future desertification (e.g., Goswami and Ramesh 2008).

Land-surface processes affect climate through the exchange of heat, moisture, and momentum between the earth's surface and the atmosphere. Land use/land cover changes over northwestern India (i.e., from croplands to desert), by altering the surface water and energy budgets through changes in (among the others) albedo, soil moisture, surface roughness, are expected to have significant impacts on monsoon hydroclimate, not necessarily confined to the local region. A global perspective of the impact of land-use changes on climate is given by Pielke et al. (2002) and Pielke et al. (2007).

Among the various effects of vegetation degradation, two factors have been shown to have a major influence on the energy and water balance: (i) an increase in surface albedo, and (ii) a decrease in surface roughness. An increase of albedo leads to less solar radiation absorbed by the ground (thus surface cooling) and to a net radiation decrease at the top of the atmosphere, which induces compensating subsidence aloft and inhibits precipitation development. Surface roughness reduction negatively affects the fluxes of momentum, heat, and moisture from the surface to the atmosphere, and therefore convection too. Furthermore, soil moisture decrease by vegetation reduction affects evapotranspiration and therefore moisture availability in the atmosphere, which in general also negatively impact precipitation. The three mechanisms sustain positive feedback loops, since in all three cases precipitation decrease in turn leads to more desertification. It is also clear that in nature all these processes interact with each other and have positive and negative feedbacks with other processes too (e.g., Nicholson 1988; Warner 2004).

The impact of vegetation changes on climate has been widely investigated, especially for the Sahel area. Charney (1975) and Charney et al. (1977) first investigated the effect of overgrazing on land-surface albedo over northern Africa and highlighted a positive feedback mechanism acting to perpetuate drought conditions (e.g., Dickinson 1992). The importance of latent-heat fluxes over vegetated areas was subsequently noted (e.g., Ripley 1976). More complex modeling studies confirmed these findings (e.g., Ellsaesser et al. 1976; Chervin 1979; Sud and Fennessy 1982; Laval and Picon 1986). Other studies (e.g., Shukla and Mintz 1982; Sud and Fennessy 1984) focused separately on the effect of reduced evapotranspiration over Northern Africa. The combined effect of albedo and soil moisture (e.g., Sud and Molod 1988) and of surface roughness (e.g., Sud et al. 1988) has also been investigated. More realistic desertification experiments followed, where multiple parameters were simultaneously changed in the land-surface model by changing the vegetation cover (e.g., Mylne and Rowntree 1991; Lean and Rowntree 1993; Xue and Shukla 1993, 1996; Xue 1996; Dirmeyer and Shukla 1996; Zeng et al. 1996; Clark et al. 2001; Xue and Fennessy 2002; Oyama and Nobre 2004; Sen et al. 2004; Gupta et al. 2005). Almost all of these studies used a general circulation model (GCM). Furthermore, at our knowledge, the impact of desertification over the Indian Subcontinent has been addressed only by Dirmeyer and Shukla (1996), also with a low-resolution GCM.

There is almost consensual agreement among GCMs studies that land cover degradation (i.e., desertification) would result *locally* in precipitation decrease, regardless of the geographical location of the target region, together with significant changes in the circulation and of the three-dimensional thermodynamical structure of the atmosphere in

the *surrounding* areas. However, not necessarily surface temperature (surface pressure) increases (decreases) over the degraded land, leading to the formation of a surface low, since the outcome depends on the predominance of the impact of reduced absorbed surface radiation versus reduced evaporation (e.g., Dirmeyer and Shukla 1996; Oyama and Nobre 2004; Gupta et al. 2005). In principle, it is also reasonable to expect the atmospheric response to be different from region to region, depending on the relative role of local versus remote forcings on the climate of the region.

The primary goal of this work is to investigate the impact of the expanded desert over northwestern India and Pakistan on the South Asian summer monsoon hydroclimate with a state-of-the-art regional climate model. A somewhat extreme scenario is prescribed, in which all the area between eastern Pakistan and northwestern India has undergone extensive desertification due to a decrease of water availability (e.g., by retreat of the Karakorum glaciers, over-irrigation over its northern part), including a significant reduction of the Indus River flow and dry-up of its Valley (already identified as a "hot-spot" in several studies; see UNEP1998; WRI 2003; Wong et al. 2007), at least its southern sector.

This article is organized as follows: Section 2 describes the regional model, the design of the experiment and the observational data used for model verification. The control simulation is analyzed in Section 3, while the impact of desertification is discussed in Section 4. Summary and conclusions follow in Section 5.

2. Model, Experiments, and Data

2.1 WRF

The Weather Research and Forecast (WRF) model, specifically the Advanced Research WRF (ARW, version 3.1.1 released on July 31, 2009), was used in this study. Its core is based on an Eulerian solver for the fully compressible nonhydrostatic equations in flux (conservative) form, using a terrain-following hydrostatic pressure-vertical coordinate. The model has a two-nesting capability and numerous physics options. A full description of the modeling system is given in Skamarock et al. (2008). WRF has been successfully used in several works, from case studies to long-term simulations (e.g., Das et al. 2008; Zhang et al. 2008; Caldwell et al. 2009; Decharme et al. 2009; Kwun et al. 2009; Leung and Qian 2009; Qian et al. 2009; Wu et al. 2009; Routray et al. 2010).

In this study, WRF-ARW was implemented with the WRF Single-Moment 5-class microphysics scheme (WSM5; Hong et al. 2004; Hong and Lim 2006), a modified version of the Kain-Fritsch scheme for cumulus convection (Kain 2004), the spectral-band scheme (Collins et al. 2004) used in the NCAR Community Atmosphere Model (CAM 3.0) for both shortwave and longwave radiation, the fifth-generation Pennsylvania State University–NCAR (PSU–NCAR) Mesoscale Model 5 (MM5) surface-layer scheme based on the Monin-Obukhov similarity theory, the Noah land-surface model (LSM; Chen and Dudhia 2001) with soil temperature and moisture predicted at four layers, fractional snow cover and frozen soil physics, the Yonsei University (YSU) Planetary Boundary Layer model (PBL; Hong et al. 2006). This configuration represents one of the most common land-surface, surface-layer and PBL configurations used by the WRF

community. Several tests were conducted prior to the final runs in order to investigate the sensitivity of the performance of the model to the choice of cumulus, microphysics, and radiation parameterization schemes. The chosen configuration resulted in the most realistic representation of summer monsoon hydroclimate.

WRF was run at 36 km horizontal resolution with 28 vertical levels over an area spanning from Eastern Africa to Indochina in the zonal direction, and from the Equator to north of the Tibetan Plateau in the meridional direction (Fig. 1). All the significant geographical features of the area are therefore included in the domain. The large-scale initial and lateral boundary conditions were provided by the NCEP Final Analysis (FNL) 6-hourly data at 1° resolution. Observed SST was also prescribed according to the NCEP real-time global daily SST analysis (RTG_SST; Gemmill et al. 2007) and linearly interpolated to 6-hourly data. Boundary conditions are read and updated every 6 hours.

The Noah LSM is configured to use the United States Geological Survey (USGS) 24-category land use dataset and a 16-category soil texture dataset based on the FAO maps, both interpolated to the model grid from the original 2 arc minute (~3 km) horizontal resolution. Heterogeneous vegetation greenness fraction and background surface albedo data are taken from monthly climatological datasets at 0.144° horizontal resolution provided by National Centers for Environmental Prediction (NCEP; Gutman and Ignatov 1997; Csiszar and Gutman 1999). The dominant vegetation types over northwestern India are represented in Fig. 1.

All the simulations were carried out for the year 2006, which was characterized by normal monsoon rainfall over India as a whole (Jayanthi et al. 2006). The desert impact was investigated by conducting two types of experiments, each consisting of a 4-member

ensemble of 7-month continuous simulations initialized on successive days of February (00Z February 1, 2, 3, 4) and running until 00Z September 1: the control run (CTL), and the desertification scenario (DES). In the latter case, the area of the Thar Desert was extended by changing the vegetation type over a defined region (delimited by the blue contour in Fig. 1, which approximately encloses the Indian States of Gujarat, Rajasthan, Haryana, and Punjab, and the eastern territories of the Pakistan Provinces of Sindh and Punjab; the extended area is roughly nine times the original area of the Thar Desert) to barren or sparsely vegetated (class 19). Correspondingly, vegetation fraction, roughness length and albedo were modified too. Vegetation fraction and albedo of the expanded desert were assigned by attributing to all points the average values prescribed over the actual Thar Desert in the input FNL data. The former is constant throughout the year (at 0.01, that is 1%), the latter varies between 0.23 (fall and winter) and 0.25 (spring), with an average March-August value of 0.24. For comparison, CTL albedo over the expanded desert area averages to 0.16 over the Indus plain and to 0.21 over the eastern sector during the simulated months (with little month-to-month variation). The replacement of the original land-cover with desert land is thus increasing albedo mostly on the western sector (+0.08 on average). Roughness length is prescribed according to table values and it is fixed at 0.01 m for class 19 (to be compared to the table values ranging between 0.05-0.15 m for class 2, and 0.01-0.05 for class 8; see Fig. 1). By changing vegetation type, several other parameters in the LSM are automatically changed according to table values, such as root depth (reduced to the upper soil layer), stomatal resistance, leaf area index, emissivity. The initial value for soil moisture was assigned from the FNL data in the CTL simulations; in the DES runs, soil moisture was initialized in the same way as for

vegetation fraction and albedo to represent widespread desert conditions (only the moisture in the upper layer is actually used in the desertification scenario given the reduced root depth). Since the area is already very dry during springtime, soil moisture is actually reduced only slightly (few percent) over the original non-desert area, and it is expected that soil moisture will rapidly adjust to equilibrium values. Indeed, to check the effect of soil moisture initial values, few simulations were also repeated without correcting the initial soil moisture over the expanded desert. The results were only slightly different, attesting the secondary impact of soil moisture *initial* anomalies on the results for these specific experiments.

This work should be considered as a pilot study, as we focus only on one particular year. It is fair to notice that other regional and large-scale factors (e.g., SST, land-surface conditions) affect land-atmosphere interactions over the investigated area and the subsequent monsoon evolution as well, and that their impact may vary from year to year. However, these factors are expected to modulate the response, with the desert-driven anomalies qualitatively consistent with the findings reported below, and it is reasonable to consider the following discussion to be valid regardless of the simulated year. The first two months of the simulations were considered as spin-up and were discharged. The results are presented in terms of ensemble averages of the two experiments. The significance of the difference DES-CTL was evaluated by means of the Student's *t*-test.

2.2 Observational Data

Atmospheric and surface variables are compared to the driving FNL data and to the European Centre for Medium-Range Weather Forecasts (ECMWF) Interim Reanalysis

(ERA-Interim, ERAI in the figures; Simmons et al. 2006) daily and monthly data at on a 1.5° x 1.5° grid and at 37 vertical isobaric levels obtained from the ECMWF data portal.

Precipitation observations came from several datasets: the Tropical Rainfall Measuring Mission (TRMM) 3B42 daily and 3B43 monthly datasets both at 0.25° resolution (Huffman et al. 2007), the Global Precipitation Climatology Project (GPCP) version 2.1 2.5° x 2.5° monthly average (Adler et al. 2003) and version 1.1 1° x 1° daily (1DD; Huffman et al. 2001) precipitation, the University of Delaware (UDEL) gridded monthly station land precipitation version 2.01 at 0.5°x0.5° resolution (Matsuura and Wilmott 2009a; data downloaded from the web site: http://jisao.washington.edu/data/ud/), and the Asian Precipitation-Highly-Resolved Observational Data Integration Towards Evaluation of the Water Resources (APHRODITE's Water Resources) 0.5° x 0.5° daily gauge precipitation over Monsoon Asia version 1003R1 (Yatagai et al. 2009).

Observed surface temperature was also obtained from UDEL (Matsuura and Wilmott 2009b).

3. Model Validation

As first step, the performance of the model in simulating the mean summertime (June-August, JJA; i.e., the mature phase of the monsoon) hydroclimate over South Asia is evaluated against observations and reanalysis data.

Seasonal (June-September) precipitation, for the country as a whole, was 100% of the climatological average (87% in June, 98% in July, and 107% in August). However, the monsoon went through a series of wet and dry phases: an early onset with above-

normal precipitation, a long break period in the second and third weeks of June (due to anomalous subsidence over the Indian Subcontinent caused by above-normal SSTs and enhanced convection over the equatorial Indian Ocean), a recovery until a new hiatus during the second and third weeks of July, followed by a long active phase until September. June-August rainfall was normal (above normal) for central India (western regions, including Gujarat and Rajasthan), below normal for much of the northern and, especially, northeastern regions (Jayanthi 2006; see also the web at: http://www.tropmet.res.in/~kolli/mol/Monsoon/frameindex.html).

CTL captures the main features of the observed JJA precipitation amounts and distribution (Fig. 2), and it is in reasonable agreement with observational datasets over most of the domain. The orographic precipitation along the Western Ghats (and its associated shadow effect over southern India), the Himalayas and over northeastern India, as well as the core over central India and the deficient rainfall at the north, are well-simulated. The westward limit of precipitation, with the minimum over the Thar Desert region, is realistic. However, CTL overestimates the maximum over Indochina (indeed overestimated also by ERA-Interim, while TRMM shows ocean-locked precipitation) and also produces excess precipitation over the equatorial Indian Ocean and off the Western Ghats.

The time evolution of the observed and simulated daily precipitation, averaged between 75° and 95°E (the core region of the Indian monsoon), is shown in Fig. 3. The model realistically simulated most of the precipitation events and the onset of the monsoon by the end of May, as well as the northward extension of precipitation during the mature phase of the monsoon. There is however a certain amount of disagreement on

the location of the northern limit of precipitation in the second half of May (15°-20°N instead of the observed 25°N) and during the dry period in the first half of June, which appears to be more intense in CTL than in observations. The excess precipitation along the equatorial Indian Ocean is also evident as an almost constant feature throughout the season.

Water vapor transport is a very important source of moisture and precipitation for the monsoon and Fig. 4 shows that CTL is in remarkable agreement with observations both in terms of magnitude and distribution of moisture fluxes. Convergence tends to be overestimated along the equatorial Indian Ocean (associated with the meridional gradient of the *v*-component of the wind) and over the Maritime Continent (excessive zonal wind), generating the excess precipitation. CTL appears to produce a stronger cyclonic circulation over northwestern India (presumably affected by orography) which advects dry desert air from the Middle East (see the slight precipitation deficit in Fig. 2).

The lower tropospheric circulation, represented by the 850-hPa winds, together with the middle tropospheric (i.e., 500 hPa) vertical motion allow to better estimate the model's dynamical skill in relation to precipitation and moisture fluxes distribution (Fig. 5). The agreement is certainly satisfactory, although there are some regional deficiencies. As noted above, the excess precipitation over Indochina is associated with stronger converging wind and more intense upward motion than observations. In the Arabian Sea, the Somali jet is confined to lower latitudes, with the northerly dry subsiding flow from the Middle East infiltrating over northwestern India and Pakistan (see also Fig. 6). This anomaly allows more radiation to reach and heat the ground (not shown), with a consequent deeper core of the low in the sea-level pressure field (Fig. 6). Sea level

pressure is lower than in observations due to a warm bias over the land-mass (not shown); note however that the horizontal gradient, which is what actually counts, is in good agreement.

The model performance over two key regions (i.e., the semi-arid region over northwestern India and the maximum precipitation area over Central India, respectively) can be estimated looking at vertical profiles of vertical velocity and relative humidity (Fig. 7). May and July are chosen because the former is the month before the monsoon onset, when the conditions are set up for the arrival of precipitation, while the latter is the month of full development of the monsoon, with strong convection and widespread precipitation. The simulated profiles are realistic and compare well with observations, with the main features consistently reproduced, especially over Central India. CTL tends to generate enhanced subsidence over northwestern India, especially in July, which results in lower relative humidity. As a result, the simulated precipitation is also deficient (cf. Fig. 2).

In general, the model is shown to realistically reproduce most of the features of monsoon hydroclimate over South Asia, and it is therefore adequate to carry out the desertification sensitivity experiment.

4. Impact of the Expanding Desert

Changes in the main components of the atmospheric water balance induced by the expanded desert during JJA are shown in Fig. 8, which displays the anomalies (i.e., differences DES-CTL) of precipitation, evaporation, vertical integrated moisture fluxes, and upper-layer soil moisture. The most remarkable feature is the large-scale significant

response of monsoon hydroclimate to the increased desert, which extends well-beyond the area of the imposed forcing across the whole Indian Subcontinent. *Locally*, the replacement of current vegetation with bare ground induces significant and consistent negative anomalies for all variables, further reinforcing the forcing mechanism. *Regionally*, the response is even more intense and is characterized by a somewhat northwest-southeast band pattern with an evident large-scale anomalous anticyclone over northeastern India. This flow opposes the southeasterly moisture advection from the Bay of Bengal toward the Indo-Gangetic Plain, and brings moist air toward the southern part of the peninsula (a relatively dry region under the rain shadow effect; see Figs. 2 and 4). Precipitation is therefore reduced (increased), respectively. Interaction with orography (the eastern Himalayas) over northeastern India and Burma enhances the westerly flow; convergence and precipitation is then generated when this current impacts on the mountains of Indochina (see Fig. 1). Evaporation and soil moisture anomalies are linked to precipitation anomalies, being for example strongly positive over south-central peninsular India and mostly negative over the northern regions.

Interestingly, surface skin temperature (not shown) has a dipole pattern over the desert region, with, broadly speaking, decreased (increased) values over the west (east and northeast) sector, the separation line being approximately along 72°E. The heating is not however communicated to the atmosphere given the clear reduction of sensible heat flux (as we will see hereafter), resulting in atmospheric cooling above the entire desert (Fig. 10c). The JJA average anomalies of various components of the surface energy budget are represented in Fig. 9. Downward shortwave radiation increases, not only over the desert but also over the central regions, in agreement with cloudiness reduction (see

Fig. 10d) and precipitation decrease. Associated with increased precipitation (and cloudiness), surface downward shortwave radiation is reduced over Indochina and, consequently, upward shortwave radiation too. Upward shortwave radiation increases especially over the expanded desert as a result of the increased albedo. Both longwave components decrease over the desert: the upward component (dominating the net longwave balance) because of surface cooling (to the west) and the effect of the variation in surface emissivity (lower for desert), which overcomes the slight warming (to the east); the downward component due to cloudiness decrease. The net radiation budget is negative to the west and positive above the area of the original Thar Desert, reflecting the pattern of albedo change between CTL and DES (which can be estimated by the ratio between the upward and the downward component of shortwave radiation, i.e. SWUPB/SWDNB in Fig. 9). Sensible and latent heat fluxes are both significantly affected by the reduced surface roughness (which decreases the surface exchange coefficient) and decreased vegetation in the desertification experiment: sensible heat strongly decreases (slightly increases) to the west (east), while latent heat decreases everywhere, especially to the east. The maximum (negative) values of sensible and latent heat fluxes are comparable. These patterns suggest that different processes are competing over this region, the relative predominance coming from the distribution of precipitation in CTL, in particular the increase to the east. On the west, where precipitation is very scarce (cf. Section 1 and Fig. 2), the effect of albedo change prevails, leading to surface cooling and reduced sensible heating. Latent heat reduces too (but not significantly) because of lower surface roughness (and reduced vegetation). On the (slightly) wetter east, precipitation is significantly reduced in the desertification experiment, leading to a

more significant soil moisture deficit and evaporation decrease (see Fig. 8). In turn, the marked reduction of evaporative cooling offsets the effect of albedo change, leading to a warmer ground (and consequent positive anomalous sensible heat flux).

Both longwave components are positive over eastern India, reflecting the positive temperature anomaly (see Fig. 10) and the cloudiness decrease, with the upward component again dominating in the net balance. The net radiation budget is positive over central India and negative over northeastern India and Indochina, in both cases dominated by the contribution of the downward shortwave anomaly (therefore by cloudiness anomalies). It is intuitive that over south-central India, for example, increased latent heat flux is associated with higher soil moisture and larger precipitation, which in turn cools the ground and reduces sensible heat flux.

Sea-level pressure (Fig. 10) shows a clear dipole pattern, with positive anomalies across India toward southern Indochina and negative to the north. The correspondence with the pattern of anomalous vertical motion is evident over central India. Note that pressure increases all over the desert area, including over areas of (albeit slight) warming, indicating that the evaporation suppression and attendant processes (Sud and Fennessy 1984), which would lead to a thermal low, are not sufficiently strong. Subsidence anomalies take place over all northwestern India above 550 hPa, while in the lower Troposphere it is confined to the north since the northwesterly subsiding flow impacts almost perpendicularly on the Aravalli Range (see Fig. 1) generating orographic-forced uplift[2].

[2] The Aravalli Range, despite its relatively modest elevation, can indeed play an important role in organizing the spatial distribution of rainfall over northwestern India, as suggested by Chao and Barros (2007).

Noticeable is a core of high pressure located over eastern India (which is associated with moisture divergence and precipitation suppression, see Fig. 8). The anticyclonic anomaly extends throughout the whole atmospheric column up to 200 hPa (where it is replaced by a large-scale anomalous cyclone centered over the Tibetan Plateau), with the most intense circulation at 700hPa. The whole column is drier and cooling is also seen above 700 hPa, clearly related to the decrease of diabatic heating. To keep atmospheric thermal balance, adiabatic warming increases, and, indeed, large-scale anomalous subsidence dominates at all levels, with peak at 500 hPa. In the boundary layer, a positive temperature anomaly originating from the heated ground (as a result of reduced cloudiness) exists, which contributes to damping the downward motion.

Figure 11 helps to relate the circulation anomaly over eastern India with the desert forcing to the west and suggests a possible mechanism to explain the regional-scale response to the expanded desert: the dry air subsiding to the west is advected toward northeastern India, where it opposes the prevailing cyclonic southeasterly humid flow (indeed drier conditions are seen throughout the whole Troposphere west of 90°E). The cyclonic circulation weakens (i.e., an anomalous anticyclone is formed), which reduces precipitation and latent heat release in the middle troposphere. Fewer clouds allow more radiation to reach the ground, where a positive temperature anomaly forms. The linearized vorticity equation, and in particular the zonal advection of relative vorticity by the mean wind, can be helpful in interpreting the observed anomalous pattern: Anomalous widespread subsidence and lower-tropospheric anticyclonic (i.e., negative relative vorticity) circulation (to its west) appears from May over the extended desert region, in agreement with vorticity balance. The westerly zonal mean wind advects the

negative vorticity anomaly to the east, where it creates a negative anomaly over eastern India (from June) which leads to reduced upward motion. The low-level anomalous flow, as mentioned above, impacts on the mountains of Indochina together with the humid air coming from the Bay of Bengal and is deflected eastward, where strong convergence, orographic ascent and precipitation occur. The release of latent heat there warms the air at upper levels, as seen in Fig. 11c. From June onward, the altered monsoon influence to the northwest is superposed on the desert direct forcing, precluding a linear attribution analysis.

5. Summary and Conclusions

The impact of desertification over northwestern India (i.e., expansion of the Thar Desert around its present-day location) on the South Asian summer monsoon was studied by mean of ensemble sensitivity experiments with the ARW-WRF model. Desert conditions were prescribed by changing the distribution of vegetation types and associated parameters (e.g., albedo, vegetation greenness, roughness length, etc.) over a large area located between Pakistan and northwestern India. As previously shown by other desertification studies (e.g., Xue and Shukla 1993; Dirmeyer and Shukla 1996; Xue and Fennessy 2002; Sen et al. 2004), there is a strong link between anomalous surface conditions and overlying atmospheric circulation.

Indeed, intensive exploitation of natural resources (water in particular) has been taking place over the relatively dry northwestern India, as a result of rapid population growth and expansion and, as a result, the region is under the threat of future desertification. This argument provided the motivation for the present study. The

occurrence of a large-scale phenomenon such as the South Asian summer monsoon makes the problem both challenging (given the numerous feedback processes in place) and of primary interest (given the potential modification and/or redistribution of the monsoon water availability for the most populated region of the world). The area by itself is particularly complex, bounded by an extensive mountain range to the east and north, and with the ocean immediately to the south.

Our findings suggest that the expansion of the desert at the expense of cultivated land significantly impacts the summer monsoon hydroclimate and circulation both locally and at large scale over the whole Indian Subcontinent. Due to interactions with the surrounding topography and feedbacks within the developing monsoon, the effect of an expanded desert leads, for example, to both increase and decrease of monsoon precipitation, depending on the specific area considered.

Overall, the key results can be summarized as follows (see also the schematic in Fig. 12):

- *Locally*, the atmospheric water cycle weakens, since precipitation, evaporation, and atmospheric moisture convergence all decrease. Soil moisture and runoff reduce too. Air temperature cools due to the overall dominant impact of albedo increase and because of the reduction of surface turbulent fluxes. Subsidence is generated by thermodynamic balance, which increases sea-level pressure and induces a low-level northwesterly flow over northern India.
- *Regionally*, moisture advection from the head of the Bay of Bengal towards northern India is weakened by the anomalous horizontal circulation set up by the desert to the west. This reduces precipitation over eastern India, with consequent

cooling of the middle Troposphere by decrease of the latent-heat release and related vertical motion, with the formation of an anomalous anticyclone. The ground heats up.

- *At larger scale,* the cooling over northwestern India extends throughout the Troposphere, and the upper-tropospheric Tibetan High (specially its southwestern flank) weakens as a result of the anomalous subsidence over the desert area[3]. On the east, the anomalous northwesterly flow intensifies and is deviated toward the eastern Himalayas and Indochina. Orographic uplift and precipitation is generated.

Interestingly, the increase (decrease) of June-August precipitation in the Indian sector south (north) of approximately 15°N and the large-scale cooling with a resulting negative 850-200 hPa thickness anomaly centered over northwestern India found here bear resemblance with the findings of Dirmeyer and Shukla (1996).

The latent-heat flux seems to play a secondary role compared to sensible heat flux over Asia, given the small values even in the control case. Evaporation decrease (which, together with sensible heat flux decrease, reduces the removal of energy away from the surface) over the desert should contribute to control the cooling due to albedo increase. This feedback however appears to be sufficiently strong only over the northeastern sector of the desert region, since summertime latent heat flux in CTL is already low (~10W m^{-2}, equivalent to an evaporation ~0.3 mm day^{-1}). In some aspects, the anomalies induced

[3] Cooling of the tropospheric column and relative subsidence over the desert area occurs, partly, in the region occupied by the Tibetan High. As such, the High weakens, especially over its southwestern flank. This effect, driven by the "local" thermodynamic balance, is not at odds with the large-scale dynamical influence of the weakened monsoon: Weaker monsoon convection, as a whole, leads to a weaker Tibetan High and reduction in the widespread compensating "remote" subsidence (e.g., over the Middle-East areas to the northwest), with little bearing on subsidence to the immediate west.

locally by the expansion of the Thar Desert contrast with the findings over other regions (e.g., the Sahel), where a warming was simulated. As mentioned above, the latent heat contribution to the surface energy budget is however also higher there (e.g., Xue and Shukla 1993) due to a different original vegetation and moisture availability. Briefly, the evaporation efficiency as controlling factor of the reduction of absorbed solar radiation is quite marginal over the region investigated here (see Zeng and Neelin 1999). Topography and the geographical features of the region are also expected to play an important role and to make differences with similar experiments carried out over other areas of the world.

To our knowledge, this study is the first using a regional model and the conclusions are far from being definitive. More simulations (for example multi-year runs) are necessary to make the case robust, and, as such, these findings represent a first attempt to assess the magnitude of the impact of the expansion of the Thar Desert on the South Asian summer monsoon.

It is possible that some surface parameters in the land-surface model (e.g., surface roughness) are not properly tuned for the area investigated. It has to be noted that many of these parameters are still not known with enough confidence and their distribution is highly heterogeneous, even for the same surface type. As a result, outcomes may vary depending on the prescription of these vegetation/surface parameters. Sensitivity studies to the variation of the parameters and/or to specific processes are not numerous (e.g., Hales et al. 2004; Li et al. 2007).

Finally, desertification is responsible for the production (through wind erosion of the bare ground) and emission of large quantities of dust particles in the atmosphere,

which can then be transported at large distance. Dust aerosols are known to have important effects on the radiative balance and thus on climate, and may lead to significant feedbacks over desert areas (e.g., Rosenfeld et al. 2001). The inclusion of dust effects in land-use experiments is an important step toward a comprehensive simulation of the impact of desertification on climate (e.g., Niyogi et al. 2007; Yoshioka et al. 2007). Along the same line, we acknowledge that the expansion of the Thar Desert may occur in context of other subcontinental changes in the monsoon climate (e.g., warming of the Indian Ocean (e.g., Ihara et al. 2008)) induced by other forcings (e.g., large-scale aerosol loading over South Asia, greenhouse gas warming, etc.), which, through complex coupled feedbacks, may actually overall act in the opposite direction.

Bearing this in mind, the conclusions of this work suggest the possibility of a significant and pronounced large-scale impact of desertification over northwestern India.

Acknowledgements

The authors would like to thank: two anonymous reviewers whose comments contributed to improve the manuscript, the Computational and Information Systems Laboratory (CISL) of the National Center for Atmospheric Research (NCAR) for the computational support, and Dr E. Hugo Berbery (UMD) for helpful discussions. The authors acknowledge support of NSF-ATM-0649666 and DOE-DEFG0208ER64548 grants. The first author was also supported by the Green Fellowship Fund in Global Climate Change.

References

Adler, R. F., G. J. Huffman, A. Chang, R. Ferraro, P. Xie, J. Janowiak, B. Rudolf, U. Schneider, S. Curtis, D. Bolvin, A. Gruber, J. Susskind, P. Arkin, and E. Nelkin, 2003: The Version 2 Global Precipitation Climatology Project (GPCP) Monthly Precipitation Analysis (1979-Present). *J. Hydrometeor.*, **4**, 1147-1167.

Betts A. K., J. H. Ball, A. C. M. Beljaars, M. J. Miller, and P. A. Viterbo, 1996: The land surface–atmosphere interaction: A review based on observational and global modeling perspectives. *J. Geophys. Res*., **101**, 7209–7225.

Caldwell, P., H.-N. S. Chin, D. C. Bader, and B. Govindasamy, .2009: Evaluation of a WRF dynamical downscaling simulation over California. *Climatic Change*, **95**, 499-521. doi: 10.1007/s10584-009-9583-5.

Chang, J.-H., 1972: *Atmospheric Circulation Systems and Climates*. Oriental Publish Co., Hawaii, 328 pp.

Chao, S., and A. P. Barros, 2007: A numerical study of the hydrometeorological dryline in northwest India during the monsoon. *J. Met. Soc. Japan*, **85A**, 337-361.

Charney, J. G., 1975: Dynamics of deserts and drought in Sahel. *Q. J. Royal Meteor. Soc*., **101**, 193-202.

Charney, J., W. J. Quirk, S.-H. Chow, and J. Kornfield, 1977: A comparative study of the effects of albedo change on drought in semi-arid regions. *J. Atmos. Sci.*, **34**, 1366-1385.

Chauhan, S. S., 2003: Desertification Control and Management of Land Degradation in the Thar Desert of India. *The Environmentalist*, **23**, 219–227.

Chen, F., and J. Dudhia, 2001: Coupling an advanced land-surface/ hydrology model with the Penn State/NCAR MM5 modeling system. Part I: Model description and implementation. *Mon. Wea. Rev.*, **129**, 569–585.

Chervin, R. M., 1979: *Response on the NCAR general circulation model to changed land surface albedo*. Report of the JOC study Conference on Climate Models, GARP Pub. Ser. No. 22, WMO, 563-581.

Clark, D. B, Y. Xue, R. J. Harding, and P. J. Valdes, 2001: Modeling the impact of land surface degradation on the climate of tropical North Africa. *J. Climate*, **14**, 1809–1822.

Collins, W.D., and Coauthors, 2004: *Description of the NCAR Community Atmosphere Model (CAM 3.0)*. NCAR Technical Note, NCAR/TN-464+STR, 226pp.

Csiszar, I., and G. Gutman, 1999: Mapping global land surface albedo from NOAA AVHRR. *J. Geophys. Res.*, **104**, 6215-6228.

Das, P. K., 1962: Mean vertical motion and non-adiabatic heat sources over India during the monsoon. *Tellus*, **14**, 212-220.

Das, S., R. Ashrit, G. R. Iyengar, S. Mohandas, M. D. Gupta, J. P. Geoge, E. N. Rajagopal, and S. K. Dutta, 2008: Skills of different mesoscale models over Indian region during monsoon season: Forecast errors. *J. Earth System Sci.*, **117**, 603-620.

Decharme, B., Ottle', C., S. Saux-Picart, N. Boulain, B. Cappelaere, D. Ramier, and M. Zribi, 2009: A New Land Surface Hydrology within the Noah-WRF Land-Atmosphere Mesoscale Model Applied to Semiarid Environment: Evaluation over the Dantiandou Kori (Niger). *Adv. Meteorol.*, **2009**, doi:10.1155/2009/731874.

Dickinson, R. E., 1992: Changes in land-use. *Climate System Modeling*, K. E. Trenberth (Ed.), Cambridge University Press: Cambridge, pp. 689-704.

Dirmeyer, P. A., and J. Shukla, 1996: Albedo as a modulator on regional climate response to tropical deforestration. *J. Geophys. Res.*, **99**, 20863-20877.

Ellsaesser, H. W., M. C. MacCracken, G. L. Potter, and F. M. Luther, 1976: An additional model test of positive feedback from high desert albedo. *Q. J. R. Met. Soc.*, **102**, 655-666.

Gemmill, W., B. Katz, and X. Li, 2007: Daily Real-Time Global Sea Surface Temperature - High Resolution Analysis at NOAA/NCEP. NOAA/NWS/NCEP/MMAB Office Note, **260**, 39 pp.

Goswami, P., and K. V. Ramesh, 2008: The expanding Indian desert: Assessment through weghted epochal trend ensemble. *Curr. Sci.*, **94**, 476-480.

Gupta, A., P. K. Thapliyal, P. K. Pal, and P. C. Joshi, 2005: Impact of deforestation on Indian monsoon – A GCM sensitivity study. *J. Ind. Geophys. Union*, **9**, 97-104.

Gutman, G. and A. Ignatov, 1997: The derivation of green vegetation fraction from NOAA/AVHRR data for use in numerical weather prediction models. *Int. J. Remote Sensing*, **19**, 1533-1543.

Hales, K., J. D. Neelin, and N. Zeng, 2004: Sensitivity of tropical land climate to leaf area index: role of surface conductance versus albedo. *J. Climate*, **17**, 1459-1473.

Hong, S.-Y., and J.-O. J. Lim, 2006: The WRF Single-Moment 6-Class Microphysics Scheme (WSM6). *J. Korean Meteor. Soc.*, **42**, 129–151.

Hong, S.-Y., J. Dudhia, and S.-H. Chen, 2004: A Revised Approach to Ice Microphysical Processes for the Bulk Parameterization of Clouds and Precipitation. *Mon. Wea. Rev.*, **132**, 103–120.

Hong, S.-Y., and Y. Noh, and J. Dudhia, 2006: A new vertical diffusion package with an explicit treatment of entrainment processes. *Mon. Wea. Rev.*, **134**, 2318–2341.

Huffman, G. J., R. F. Adler, M. Morrissey, D. T. Bolvin, S. Curtis, R. Joyce, B. McGavock, and J. Susskind, 2001: Global Precipitation at One-Degree Daily Resolution from Multi-Satellite Observations. *J. Hydrometeor.*, **2**, 36-50.

Huffman, G. J., R. F. Adler, D. T. Bolvin, G. Gu, E. J. Nelkin, K. P. Bowman, Y. Hong, E. F. Stocker and D. B. Wolff, 2007: The TRMM Multisatellite Precipitation Analysis (TMPA): quasi-global, multiyear, combined-sensor precipitation estimates at fine scales. *J. Hydrometeor.*, **8**, 38–55.

Ihara, C., Y. Kushnir, and M. A. Cane, 2008: Warming Trend of the Indian Ocean SST and Indian Ocean Dipole from 1880 to 2004. *J. Climate*, **21**, 2035–2046.

Jayanthi N., M. Rajeevan, A. K. Srivastava, D. Sunitha, S. K. Roy Bhowmik, and H. R. Hatwar, 2006: *Monsoon 2006: A Report*. India Meteorological Department, Pune, 103 pp.

Kain, J. S., 2004: The Kain-Fritsch convective parameterization: An update. *J. Appl. Meteor.*, **43**, 170–181.

Kwun, J. H., Y.-K. Kim, J.-W. Seo, J. H. Jeong, and S. H. You, 2009: Sensitivity of MM5 and WRF mesoscale model predictions of surface winds in a typhoon to planetary boundary layer parameterizations. *Nat. Hazards*, **51**, 63-77.

Laval, K., and L. Picon, 1986: Effect of a change of the surface albedo of the Sahel on climate. *J. Atmos. Sci.*, **43**, 2418-2429.

Lee, E., T. N. Chase, B. Rajagopalan, R. G. Barry, T. W. Biggs, and P. J. Lawrence, 2009: Effects of irrigation and vegetation activity on early Indian summer monsoon variability. *Int. J. Climatol.*, **29**, 573-581.

Lean, J., and P. R. Rowntree, 1993: A GCM simulation of the impact of Amazonian deforestation on climate using an improved canopy representation. *Q. J. R. Met. Soc.*, **119**, 509–530.

Leung, L. R., and Y. Qian, 2009: Atmospheric rivers induced heavy precipitation and flooding in the western U.S. simulated by the WRF regional climate model. *Geophys. Res. Lett.*, **36**, L03820, doi:10.1029/2008GL036445.

Li, W., Y. Xue, and I. Poccard, 2007: Numerical investigation of the impact of vegetation indices on the variability of West African summer monsoon. *J. Met. Soc. Japan*, **85A**, 363-383.

Matsuura, K., and C. J. Willmott, 2009a: Terrestrial Precipitation 1900-2008 Gridded Monthly Time series (version 2.01). Center for Climatic Research, Department of Geography, University of Delaware, Newark (available at the web address: http://climate.geog.udel.edu/~climate/html_pages/Global2_Ts_2009/README.global_p_ts_2009.html).

Matsuura, K., and C. J. Willmott, 2009b: Terrestrial Air Temperature 1900-2008 Gridded Monthly Time series (version 2.01). Center for Climatic Research, Department of Geography, University of Delaware, Newark (available at the web address:

http://climate.geog.udel.edu/~climate/html_pages/Global2_Ts_2009/README.global_t_ts_2009.html).

Miao, S., F. Chen, M.A. LeMone, M. Tewari, Q. Li, and Y. Wang, 2009: An Observational and Modeling Study of Characteristics of Urban Heat Island and Boundary Layer Structures in Beijing. *J. Appl. Meteor. Climatol.*, **48**, 484–501.

Mylne, M. F., and P. R. Rowntree, 1991: Modelling the effects of albedo change associated with tropical deforestation. *Climatic Change*, **21**, 317-343.

Nicholson, S. E., 1988: Land Surface Atmosphere Interaction: Physical processes and Surface Changes and their Impact. *Progress in Physical Geography*, **12**, 36-65.

Niyogi, D., C. Kishtawal, S. Tripathi, and R. S. Govindaraju, 2010: Observational evidence that agricultural intensification and land use change may be reducing the Indian summer monsoon rainfall. *Water Resour. Res.*, **46**, W03533, doi:10.1029/2008WR007082.

Niyogi, D., H.-I., Chang, F. Chen, L. Gu, A. Kumar, S. Menon, and R. A. Pielke, 2007: Potential impacts of aerosol–land–atmosphere interactions on the Indian monsoonal rainfall characteristic. *Nat. Hazards*, **42**, 345-359.

Oyama, M. D., and C. A. Nobre, 2004: Climatic consequences of a large-scale desertification in Northeast Brazil: A GCM simulation study. *J. Climate*, **17**, 3203-3213.

Pielke, R. A. Sr., G. Marland, R. A. Betts, T. N. Chase, J. L. Eastman, J. O. Niles, D. S. Niyogi, and S. W. Running, 2002: The Influence of Land-Use Change and Landscape Dynamics on the Climate System: Relevance to Climate-Change Policy Beyond the Radiative Effect of Greenhouse Gases. *Phil. Trans. R. Soc. Lond.,* **360**, 1705-1719.

Pielke, R. A. Sr., J. Adegoke, A. Beltran-Przekurat, C. A. Hiemstra, J. Lin, U. S. Nair, D. Niyogi, and T. E. Nobis, 2007: An overview of regional land use and land cover impacts on rainfall. *Tellus B*, **59**, 587-601.

Qian, Y., W. I. Gustafson Jr., L. R. Leung, and S. J. Ghan, 2009: Effects of soot-induced snow albedo change on snowpack and hydrological cycle in western United States based on Weather Research and Forecasting chemistry and regional climate simulations. *J. Geophys. Res.*, **114**, D03108, doi:10.1029/2008JD011039.

Rahmani, A. R., and R. G. Soni, 1997: Avifaunal changes in the Indian Thar Desert. *J. Arid Environ.*, **36**, 687-703.

Ravi, S., and T. E. Huxman, 2009: Land degradation in the Thar Desert. *Frontiers in Ecology and the Environment*, **7**, 517-518, doi: 10.1890/09.WB.029.

Rodell, M., I. Velicogna, and J. S. Famiglietti, 2009: Satellite-based estimates of groundwater depletion in India. *Nature*, **460**, 999-1002.

Rosenfeld, D., Y. Rudich, and R. Lahav, 2001: Desert dust suppressing precipitation: A possible desertification feedback loop. *PNAS*, **98**, 5975-5980.

Routray, A., U. C. Mohanty, D. Niyogi, S. R. H. Rizvi, and K. K. Osur, 2010: Simulation of heavy rainfall events over Indian monsoon region using WRF-3DVAR data assimilation system. *Meteor. Atmos. Phys.*, **106**, 107-125.

Sen, O. L., Y. Wang, and B. Wang, 2004: Impact of Indochina deforestation on the East Asian summer monsoon. *J. Climate*, **17**, 1366-1380.

Shukla, J., and Y. Mintz, 1982: Influence of land-surface evapotranspiration on the earth's climate. *Science*, **215**, 1498-1501.

Sikka, D. R., 1997: Desert climate and its dynamics. *Curr. Sci.*, **72**, 35-46.

Simmons, A., S. Uppala, D. Dee, and S. Kobayashi, 2006: ERA-Interim: New ECMWF reanalysis products from 1989 onwards. *ECMWF Newsletter*, **110**, 25–35, ECMWF, Reading, UK (Available at web address: http://www.ecmwf.int/publications/newsletters).

Singh N., N. A. Sontakke, and H. N. Singh, 2005: *Atlas of spatial features of rainfall of India: 1871-2003, Part I.* Department of Science and Technology project "Atlas of spatial features of moisture regions and rainfall of India during 19th and 20th, centuries", Indian Institute of Tropical Meteorology, Pune, 334 pp.

Skamarock W. C., J. B. Klemp, J. Dudhia, D. O. Gill, D. M. Barker, M. G. Dudhia, X.-Y. Huang, W. Wang, and J. G. Powers, 2008: *A description of the Advanced Research WRF Version 3*. NCAR Tech. Note NCAR/TN-475+STR, 125 pp.

Sud, Y. C., and M. Fennessy, 1982: A study of the influence of the surface albedo on July circulation in semiarid regions using the GLAS GCM. *J. Climate*, **2**, 105-125.

Sud, Y. C., and M. Fennessy, 1984: Influence of evaporation in semi-arid regions on the July circulation: A numerical study. *J. Climatol.*, **4**, 383-398.

Sud, Y. C., and A. Molod, 1988: A GCM simulation study of the influence of Saharan evapotranspiration and surface-albedo anomalies on July circulation and rainfall. *Mon. Wea. Rev.*, **116**, 2388-2408.

Sud, Y. C., J. Shukla, and Y. Mintz, 1988: Influence of land surface roughness on atmospheric circulation and precipitation: A sensitivity study with a general circulation model. *J. Appl. Meteorol.*, **27**, 1036-1054.

Sud, Y. C., and Coauthors, 2009: Sensitivity of boreal-summer circulation and precipitation to atmospheric aerosols in selected regions – Part 1: Africa and India. *Ann. Geophys.*, **27**, 3989-4007.

United Nations Environment Programme (UNEP), 1998: *Land cover assessment and monitoring: Pakistan*. Environmental Assessment Technical Reports, 10-A, 50 pp, UNEP/EAP.TR/95-06 (available at the web address: http://www.rrcap.unep.org/lc/cd/html/country_reports.html).

United States Department of Agriculture (USDA), 1994: *Major World Crop Areas and Climatic Maps*. Agricultural Handbook No. 664, Washington DC, 293pp (available at the web address: http://www.usda.gov/oce/weather/pubs/Other/MWCACP/world_crop_country.htm).

Wong, C. M., C. E. Williams, J. Pittock, U. Collier, and P. Schelle, 2007: *World's top 10 rivers at risk*. WWF International. Gland, Switzerland (available at the web address: http://assets.panda.org/downloads/worldstop10riversatriskfinalmarch13.pdf).

World Resource Institute (WRI), 2003: *Watersheds of the World*. The World Conservation Union (IUCN), the International Water Management Institute (IWMI), the Ramsar Convention Bureau, and the World Resources Institute (WRI): Washington, DC, (available at the web address: http://multimedia.wri.org/watersheds_2003/index.html).

Wu, J., A. D. Del Genio, M.-S. Yao, and A. B. Wolf, 2009: WRF and GISS SCM simulations of convective updraft properties during TWP-ICE. *J. Geophys. Res.*, **114**, D04206, doi:10.1029/2008JD010851.

Xue, Y., 1996: The impact of desertification in the Mongolian and the Inner Mongolian grassland on the regional climate. *J. Climate*, **9**, 2173–2189.

Xue, Y., and J. Shukla, 1993: The influence of land surface properties on Sahel climate: Part I: Desertification. *J. Climate*, **6**, 2232-2245.

Xue, Y., and J. Shukla, 1996: he influence of land surface properties on Sahel climate. Part II: Afforestation. *J. Climate*, **9**, 3260–3275.

Xue, Y., and M. D. Fennessy, 2002: Under what conditions does land cover change impact regional climate? *Global Desertification: Do Humans Cause Deserts?*, J. F. Reynolds and D.M. Stafford Smith (Eds.), Dahlem University Press, Berlin, 59–74.

Yatagai, A., O. Arakawa, K. Kamiguchi, H. Kawamoto, M. I. Nodzu, and A. Hamada, 2009: A 44-year daily gridded precipitation dataset for Asia based on a dense network of rain gauges. *SOLA*, **5**, 137-140, doi:10.2151/sola.2009-035.

Yoshioka, M., N. M. Mahowald, A. J. Conley, W. D. Collins, D. W. Fillmore, C. S. Zender, and D. B. Coleman, 2007: Impact of desert dust radiative forcing on Sahel precipitation: relative importance of dust compared to sea surface temperature variations, vegetation changes, and greenhouse gas warming. *J. Climate*, **20**, 1445-1467.

Zeng, N., and J. D. Neelin, 1999: A land–atmosphere interaction theory for the tropical deforestation problem. *J. Climate*, **12**, 857-872.

Zeng N., R. E. Dickinson, and X. Zeng, 1996: Climatic impact of Amazon deforestation - A mechanistic model study. *J. Climate*, **9**, 859–883.

Zhang, J., W.-C. Wang, and L. R. Leung, 2008: Contribution of land-atmosphere coupling to summer climate variability over the contiguous United States. *J. Geophys. Res.*, **113**, D22109, doi:10.1029/2008JD010136.

Figure captions

Figure 1: Top: model domain and topography (m), with the blue line enclosing the area of the expanded desert in the DES experiment. Middle: annual cycle of model vegetation fraction (green; x10), and of observed surface temperature (red; °C) and precipitation (blue; mm day^{-1}) from CRU averaged over the extended desert are for the period 1979-2001. Bottom: model vegetation types (left; 2 = dryland cropland and pasture; 3 = irrigated cropland and pasture; 8 = shrubland; 19 barren or sparsely vegetated) and March-June average greenness fraction (right).

Figure 2: June-August 2006 average precipitation (mm day^{-1}) in observations, reanalysis, and the control simulation.

Figure 3: Latitudinal evolution of May-August daily precipitation (mm day^{-1}) averaged between 75°-95°E.

Figure 4: June-August moisture flux (kg m^{-1} s^{-1}) and its convergence (mm day^{-1}; shaded, positive green values representing convergence) mass-weighted vertically integrated between the surface and 100 hPa.

Figure 5: June-August 850-hPa wind (m s^{-1}) and 500-hPa vertical velocity (x10 Pa s^{-1}; shaded, positive values representing subsidence).

Figure 6: June-August sea-level pressure (hPa) and [950-700]-hPa vertical integrated specific humidity (kg m^{-2}, shaded).

Figure 7a: Vertical profile of (top) vertical velocity (Pa s^{-1}) and (bottom) relative humidity (%) for (left) May and (right) July averaged over the area (25°-29°N, 68°-74°E).

Figure 7b: Vertical profile of (top) vertical velocity (Pa s^{-1}) and (bottom) relative humidity (%) for (left) May and (right) July averaged over the area (18°-24°N, 75°-85°E).

Figure 8: JJA average difference DES-CTL for: (a) precipitation (P, mm day^{-1}), (b) evaporation (E, x10 mm day^{-1}), (c) vertically integrated mass-weighted moisture flux (kg m^{-1} s^{-1}) and its convergence (shaded, positive red, mm day^{-1}), and (d) soil moisture in the upper layer (SM1, x100 mm). The light grey hatching is for statistically significant areas at the 80% (a) and 90% (b-d) confidence level. The black contour in (a) denotes the area of the expanded desert in DES.

Figure 9: JJA average difference DES-CTL for: (a) surface downward shortwave radiation (SWDNB, W m^{-2}), (b) surface net longwave radiation (NET LWB, positive downward, W m^{-2}), (c) sensible heat flux (SHF, W m^{-2}), (d) surface upward shortwave radiation (SWUPB, W m^{-2}), (e) surface net radiation (NET RAD, positive downward, W

m^{-2}), and (f) latent heat flux (LHF, W m^{-2}). The light grey hatching is for statistically significant areas at the 90% confidence level. The black contour in (a) denotes the area of the expanded desert in DES.

Figure 10: JJA average difference DES-CTL for: (a) sea level pressure (SLP, x30 hPa), (b) 700-hPa horizontal wind (streamlines) and *p*-vertical velocity (x0.5 hPa day^{-1}, positive values upward), (c) temperature vertically averaged between the surface and 850 hPa (°C), and (d) average low and middle cloud fraction (%). The light grey hatching is for statistically significant areas at the 90% confidence level. The black contour in (a) denotes the area of the expanded desert in DES.

Figure 11: JJA average vertical/zonal cross section averaged between 24°-30°N of the difference DES-CTL for: (a) *p*-vertical velocity (shaded, x0.1 hPa day^{-1}, positive values downward) and zonal circulation (streamlines), and (b) specific humidity (shaded, x10 g kg^{-1}) and temperature (contours, x10°C). Values below orography (black area) have been masked out before averaging.

Figure 12: A schematic picture of the JJA average circulation anomalies (i.e., difference DES-CTL) over the Indian subcontinent induced by the expanded desert. The expanded desert is represented by the yellow area. The Himalayas and Tibetan Plateau are also drawn. Color circular areas represent high (red) and low (blue) pressure. Large-scale vertical motion is indicated by red (subsidence) and blue (ascent) thick arrows. Black

dotted arrows represent approximately horizontal winds (i.e., mainly associated with horizontal transport).

Figures

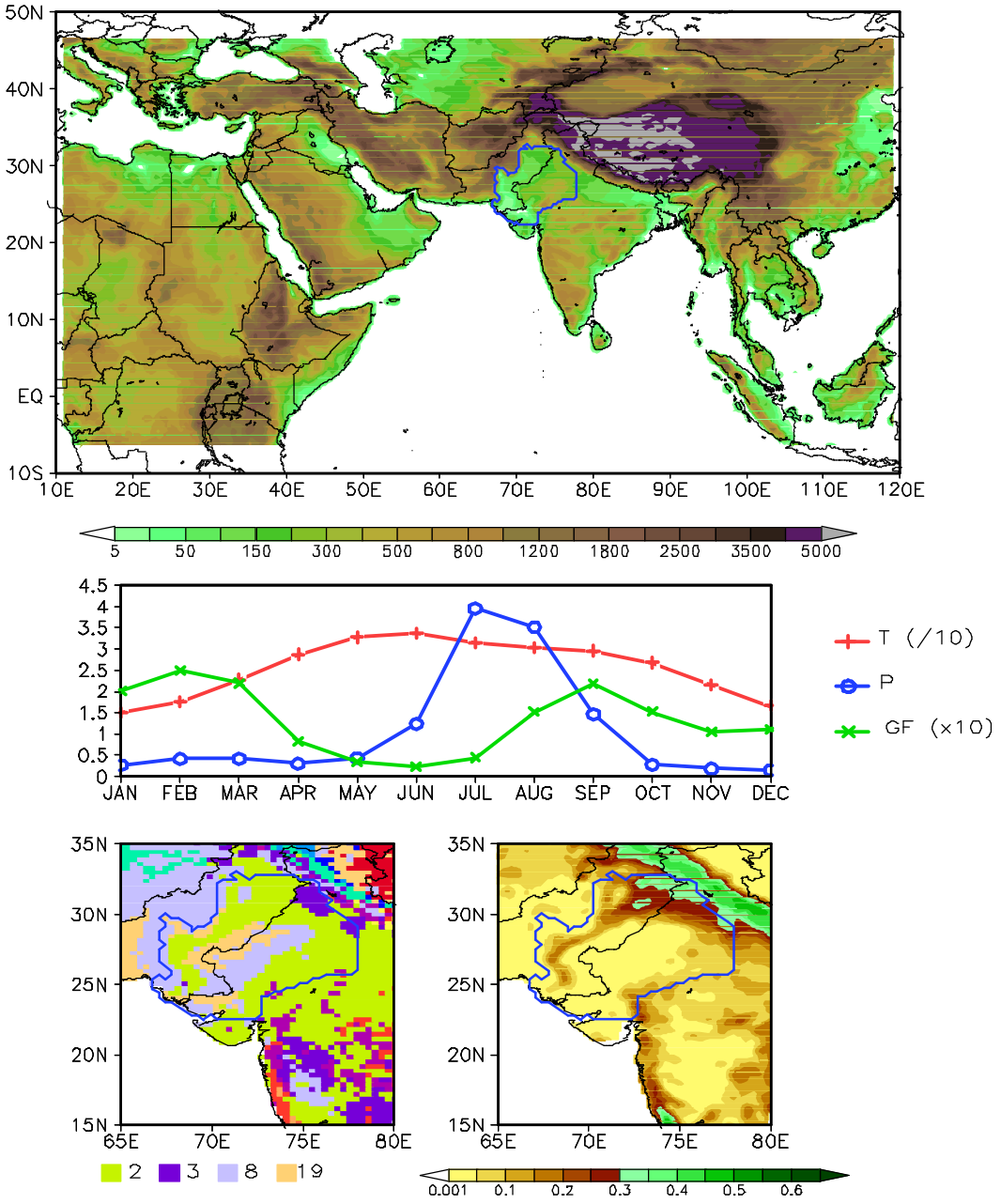

Figure 1: Top: model domain and topography (m), with the blue line enclosing the area of the expanded desert in the DES experiment. Middle: annual cycle of model vegetation fraction (green; x10), and of observed surface temperature (red; °C) and precipitation (blue; mm day^{-1}) from CRU averaged over the extended desert are for the period 1979-2001. Bottom: model vegetation types (left; 2 = dryland cropland and pasture; 3 = irrigated cropland and pasture; 8 = shrubland; 19 barren or sparsely vegetated) and March-June average greenness fraction (right).

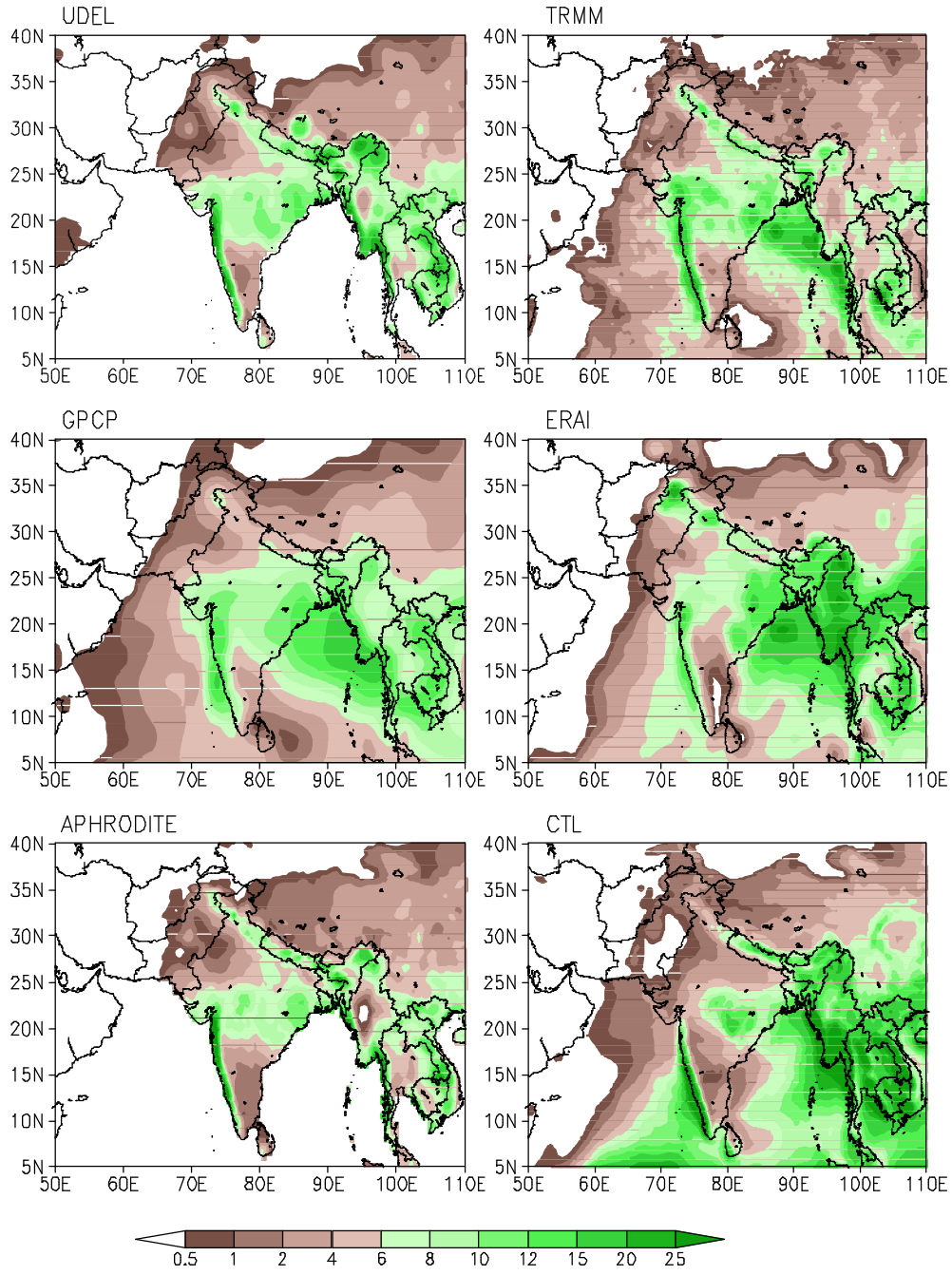

Figure 2: June-August 2006 average precipitation (mm day^{-1}) in observations, reanalysis, and the control simulation.

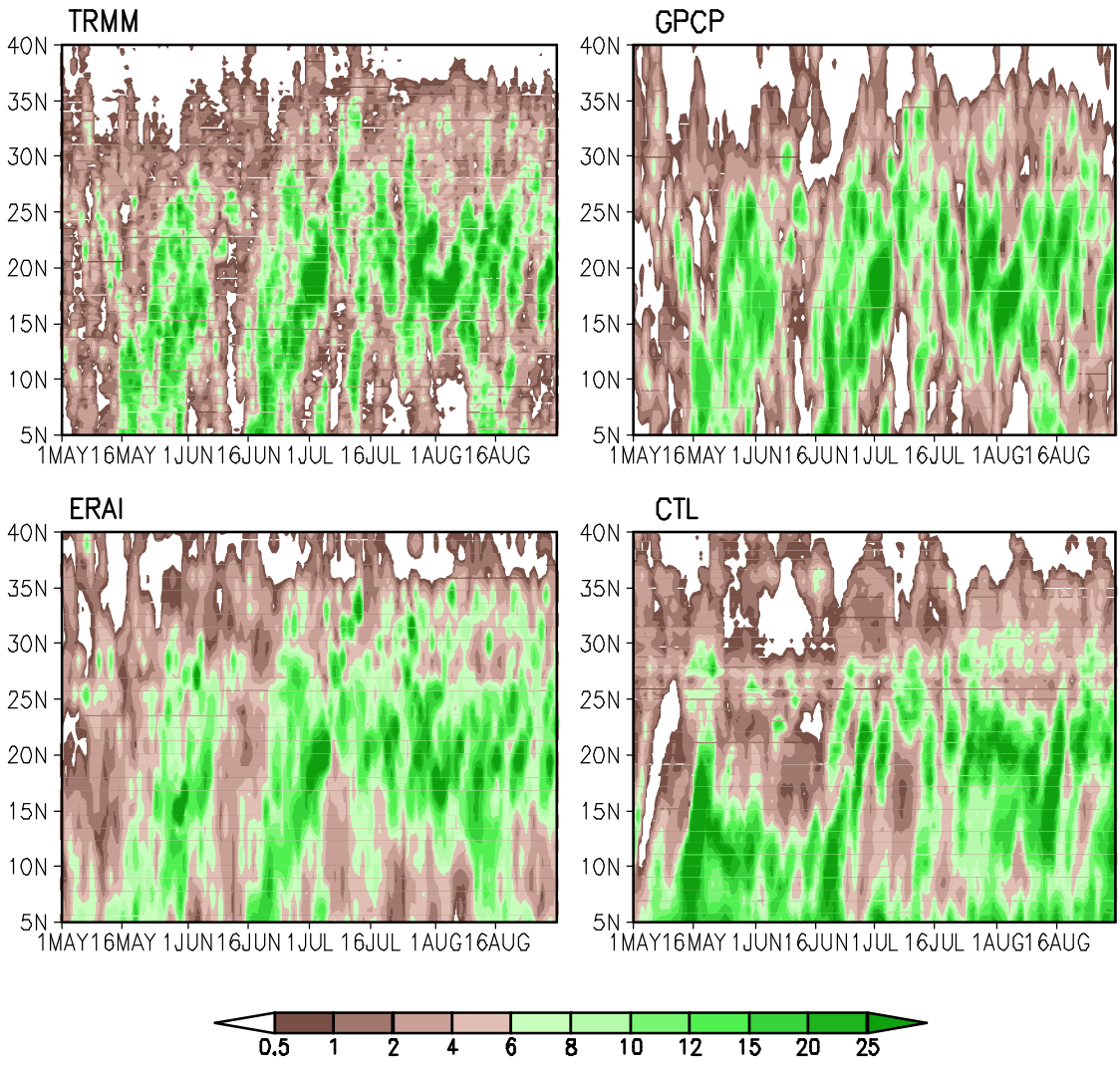

Figure 3: Latitudinal evolution of May-August daily precipitation (mm day^{-1}) averaged between 75°-95°E.

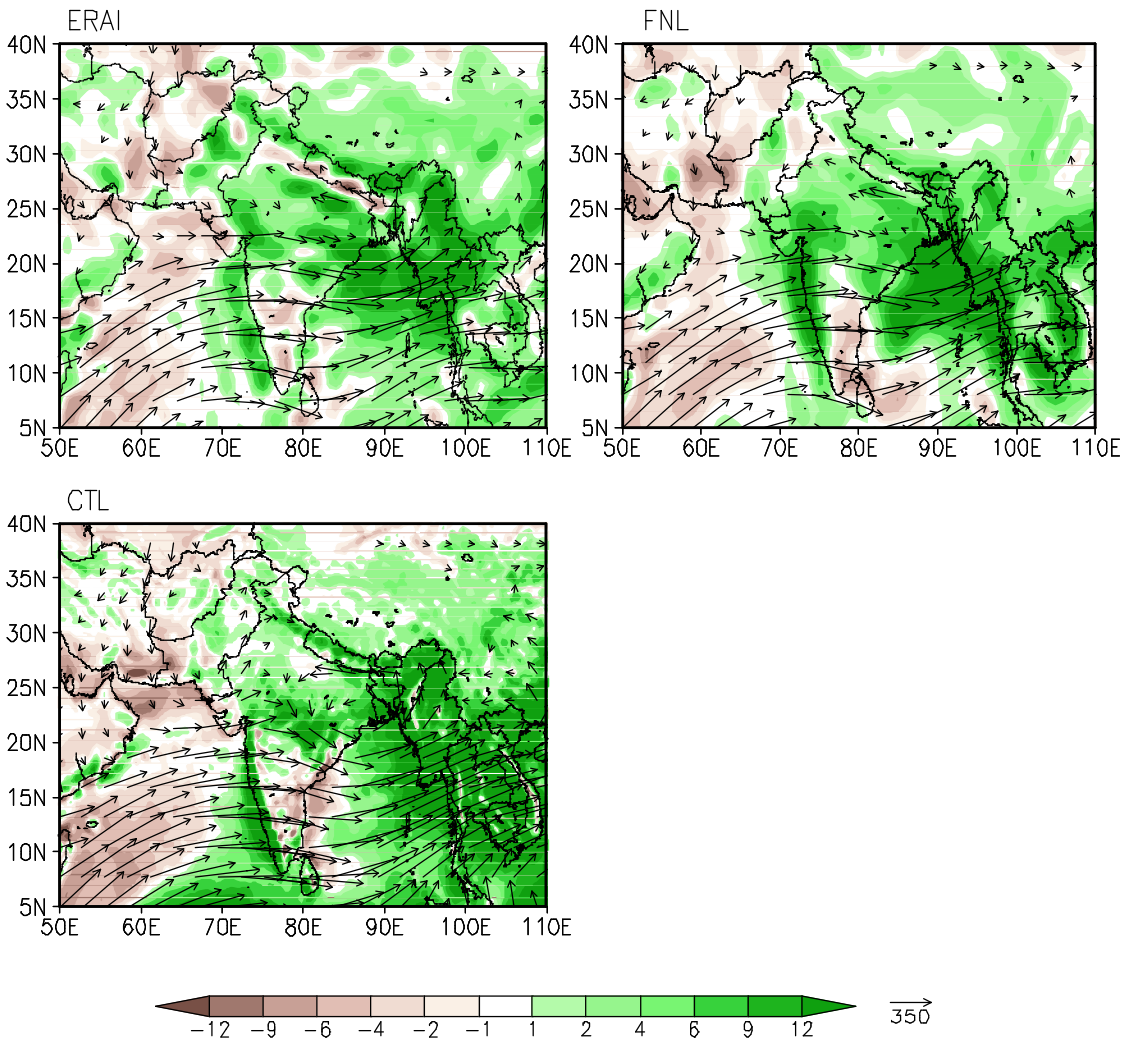

Figure 4: June-August moisture flux (kg m^{-1} s^{-1}) and its convergence (mm day^{-1}; shaded, positive green values representing convergence) mass-weighted vertically integrated between the surface and 100 hPa.

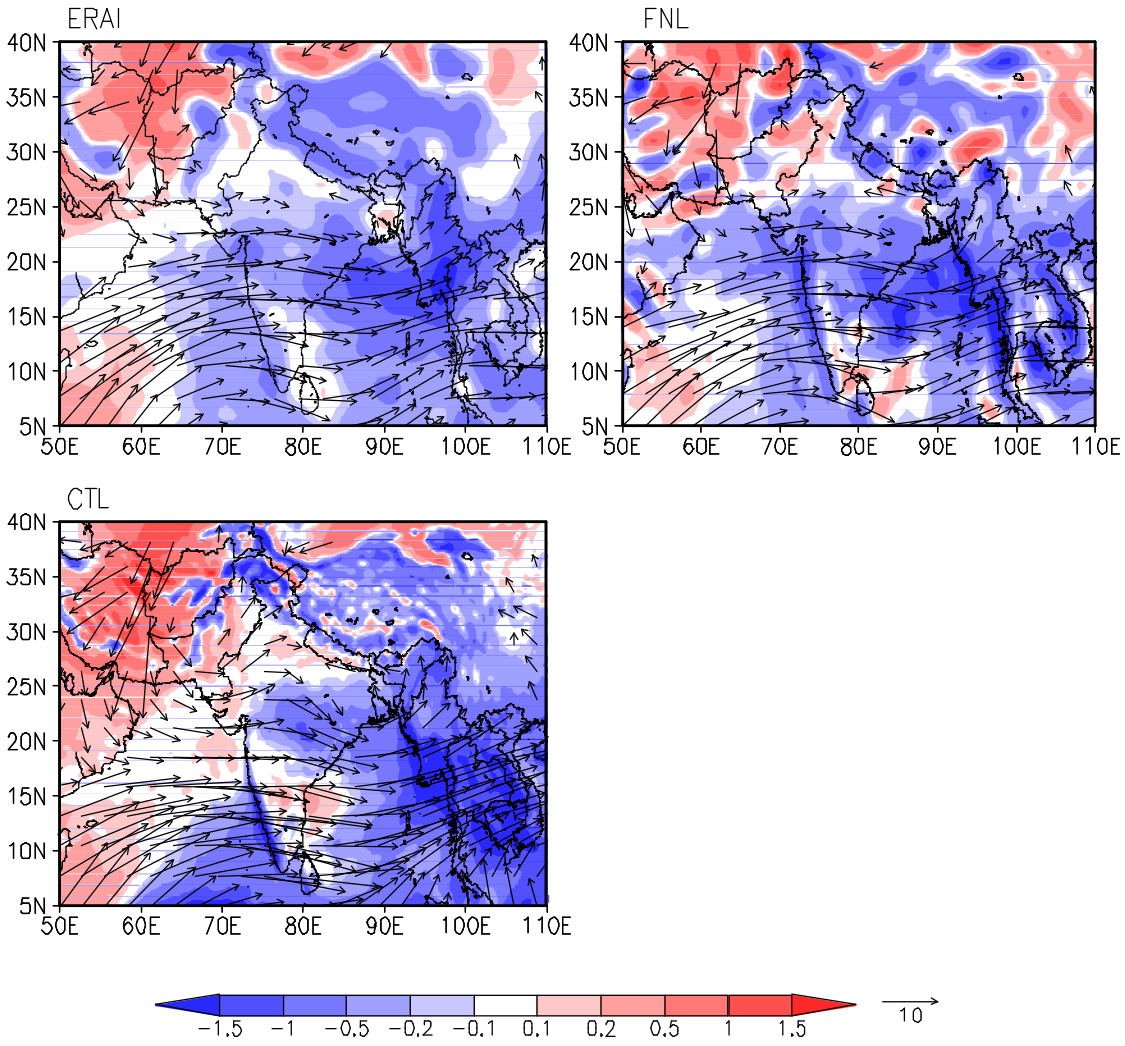

Figure 5: June-August 850-hPa wind (m s^{-1}) and 500-hPa vertical velocity (x10 Pa s^{-1}; shaded, positive values representing subsidence).

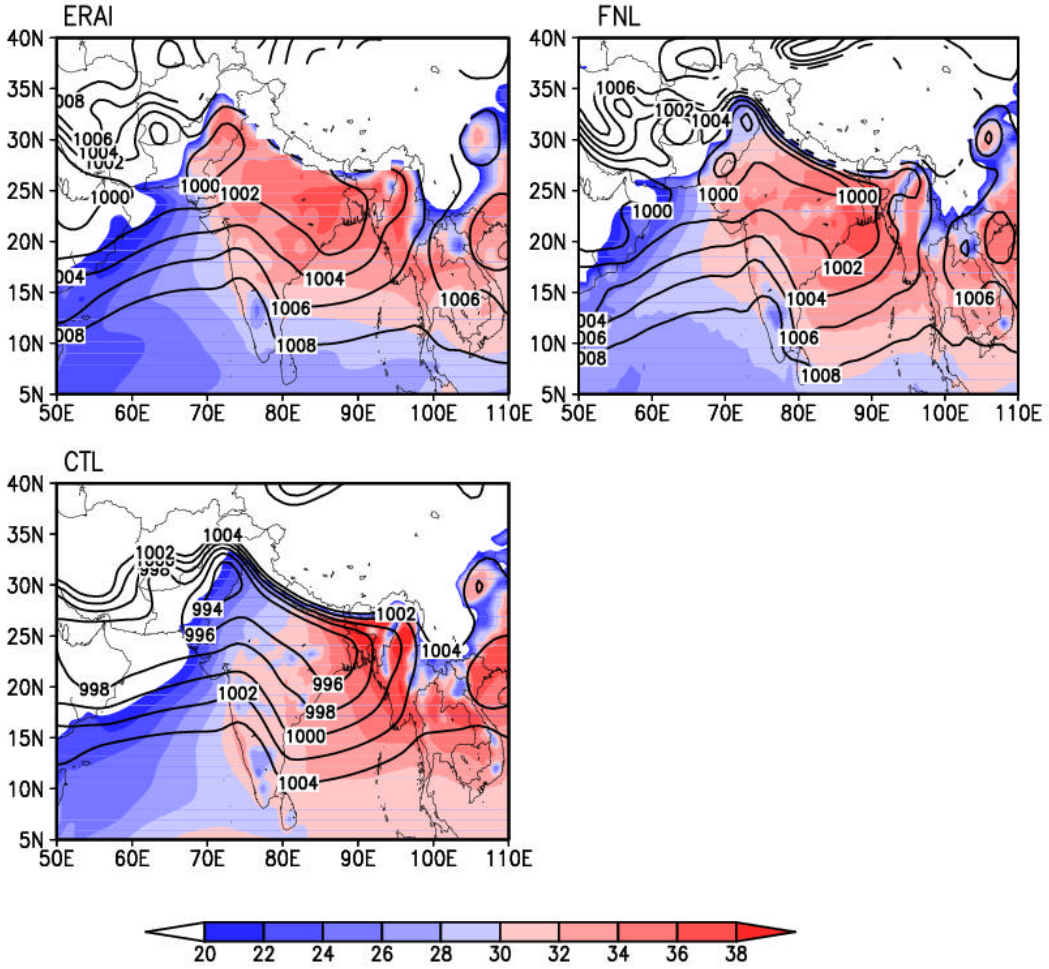

Figure 6: June-August sea-level pressure (hPa) and [950-700]-hPa vertical integrated specific humidity (kg m^{-2}, shaded).

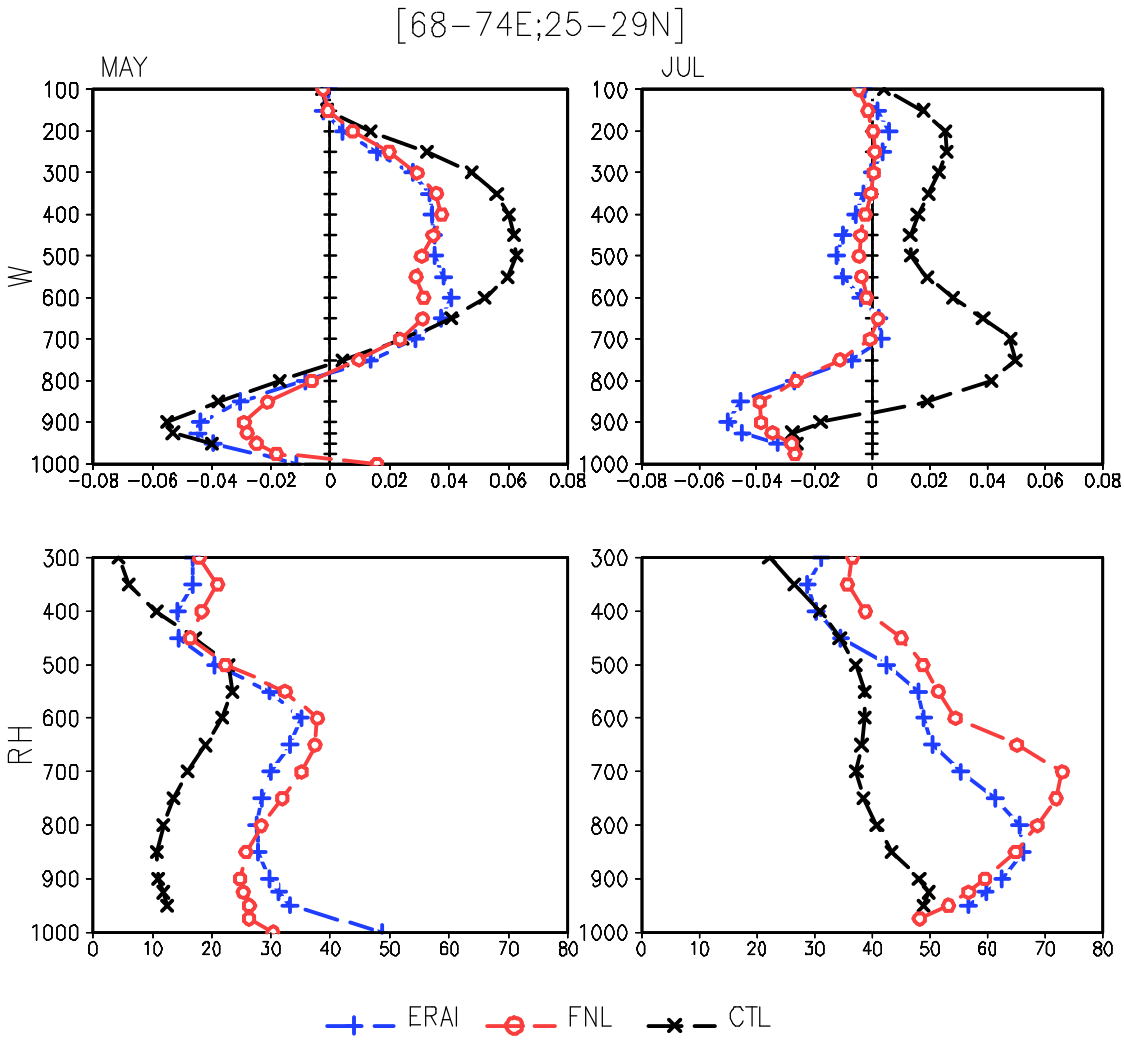

Figure 7a: Vertical profile of (top) vertical velocity (Pa s^{-1}) and (bottom) relative humidity (%) for (left) May and (right) July averaged over the area (25°-29°N, 68°-74°E).

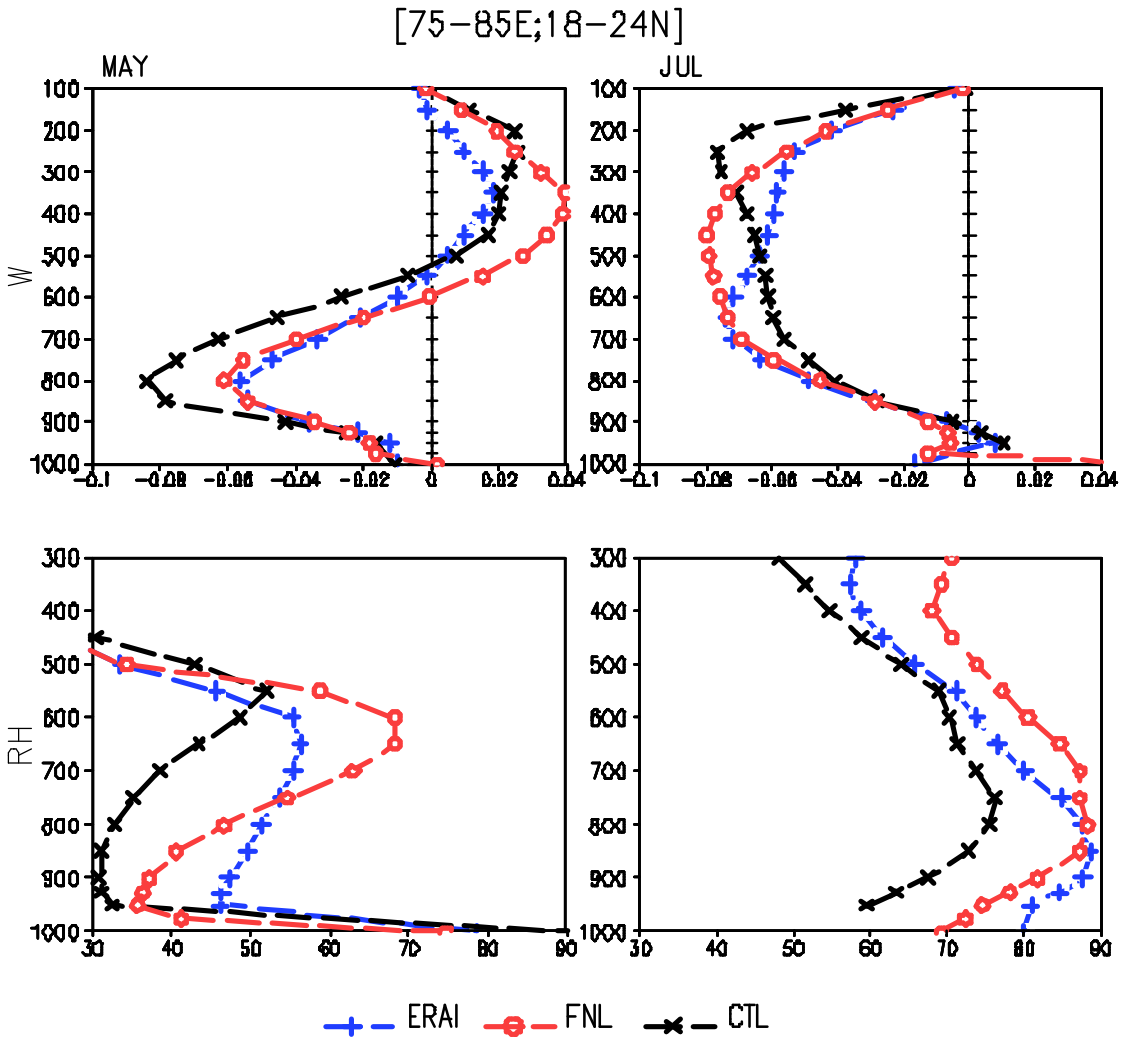

Figure 7b: Vertical profile of (top) vertical velocity (Pa s^{-1}) and (bottom) relative humidity (%) for (left) May and (right) July averaged over the area (18°-24°N, 75°-85°E).

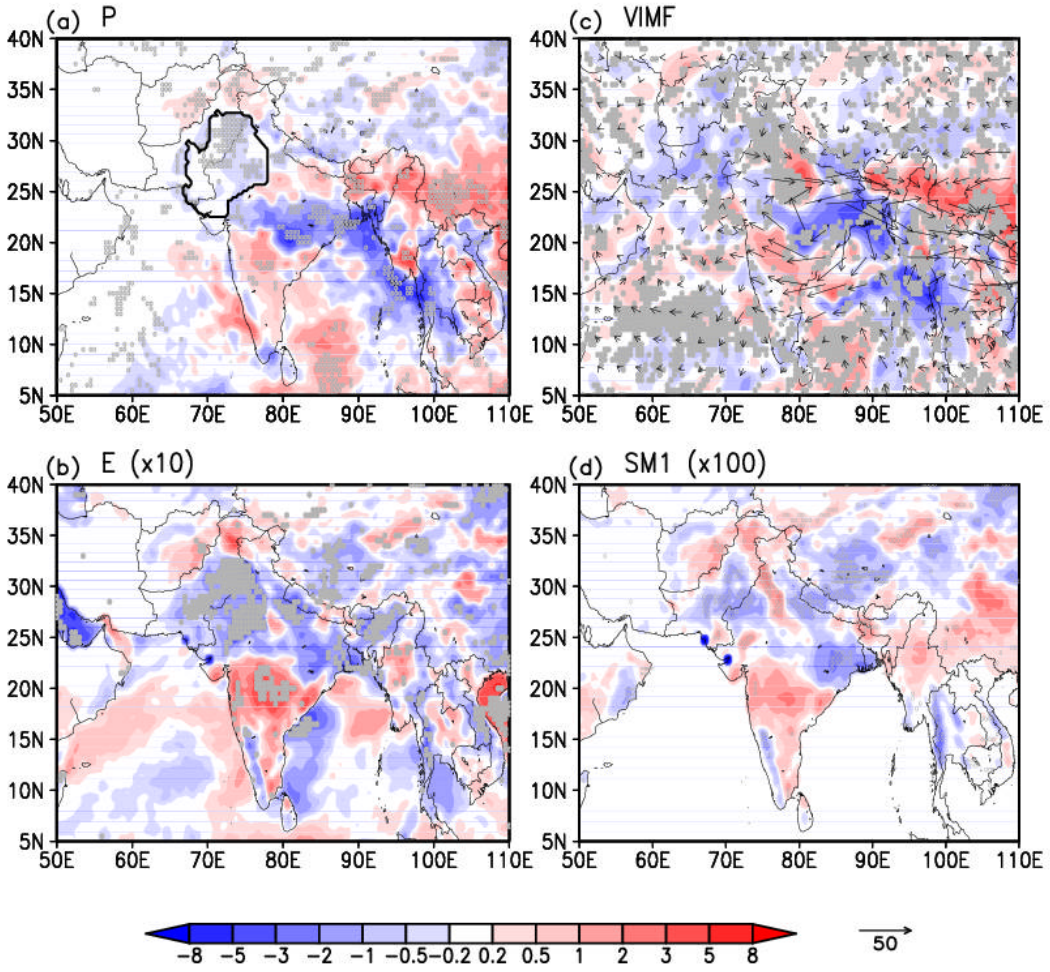

Figure 8: JJA average difference DES-CTL for: (a) precipitation (P, mm day^{-1}), (b) evaporation (E, x10 mm day^{-1}), (c) vertically integrated mass-weighted moisture flux (kg m^{-1} s^{-1}) and its convergence (shaded, positive red, mm day^{-1}), and (d) soil moisture in the upper layer (SM1, x100 mm). The light grey hatching is for statistically significant areas at the 80% (a) and 90% (b-d) confidence level. The black contour in (a) denotes the area of the expanded desert in DES.

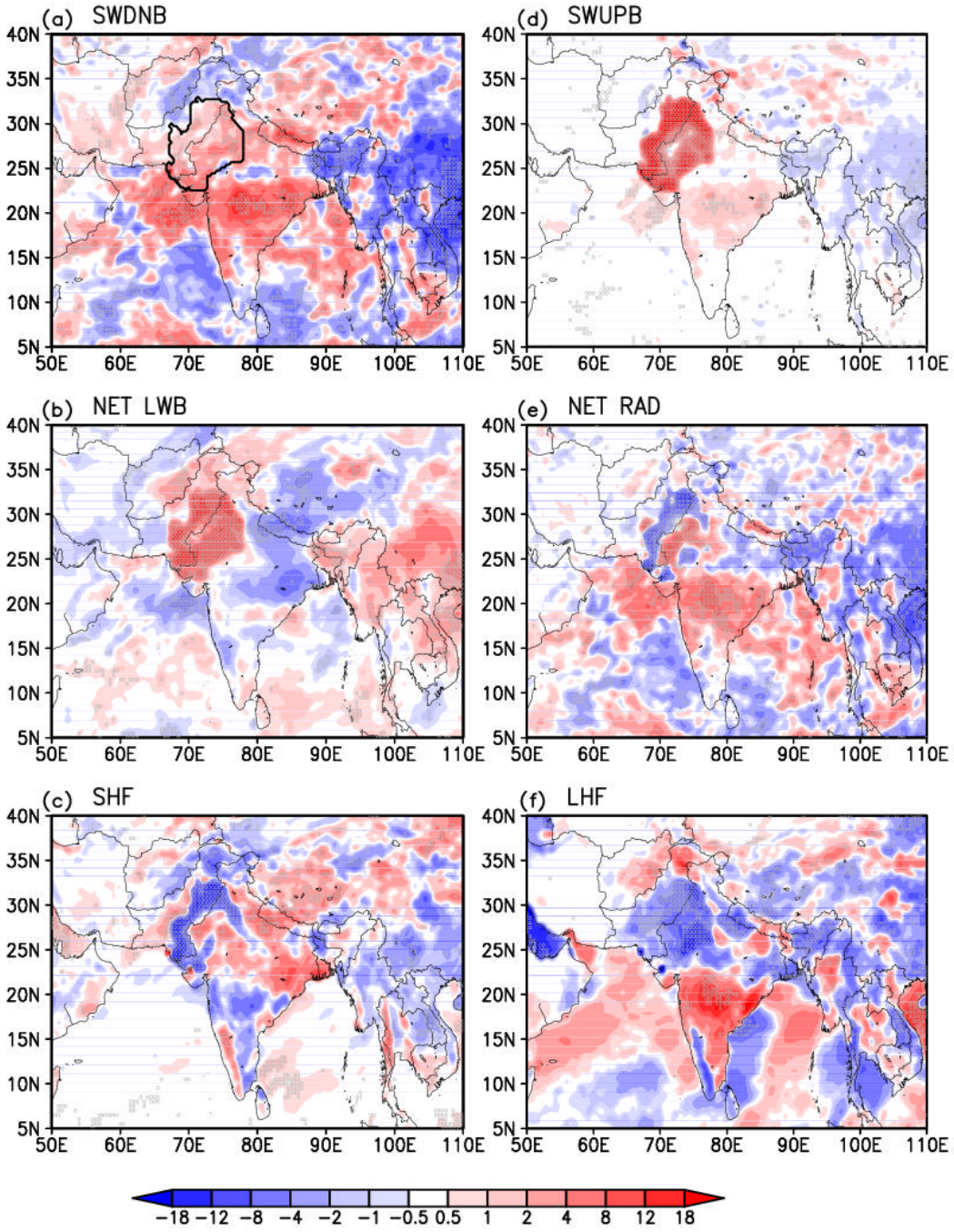

Figure 9: JJA average difference DES-CTL for: (a) surface downward shortwave radiation (SWDNB, W m^{-2}), (b) surface net longwave radiation (NET LWB, positive downward, W m^{-2}), (c) sensible heat flux (SHF, W m^{-2}), (d) surface upward shortwave radiation (SWUPB, W m^{-2}), (e) surface net radiation (NET RAD, positive downward, W m^{-2}), and (f) latent heat flux (LHF, W m^{-2}). The light grey hatching is for statistically significant areas at the 90% confidence level. The black contour in (a) denotes the area of the expanded desert in DES.

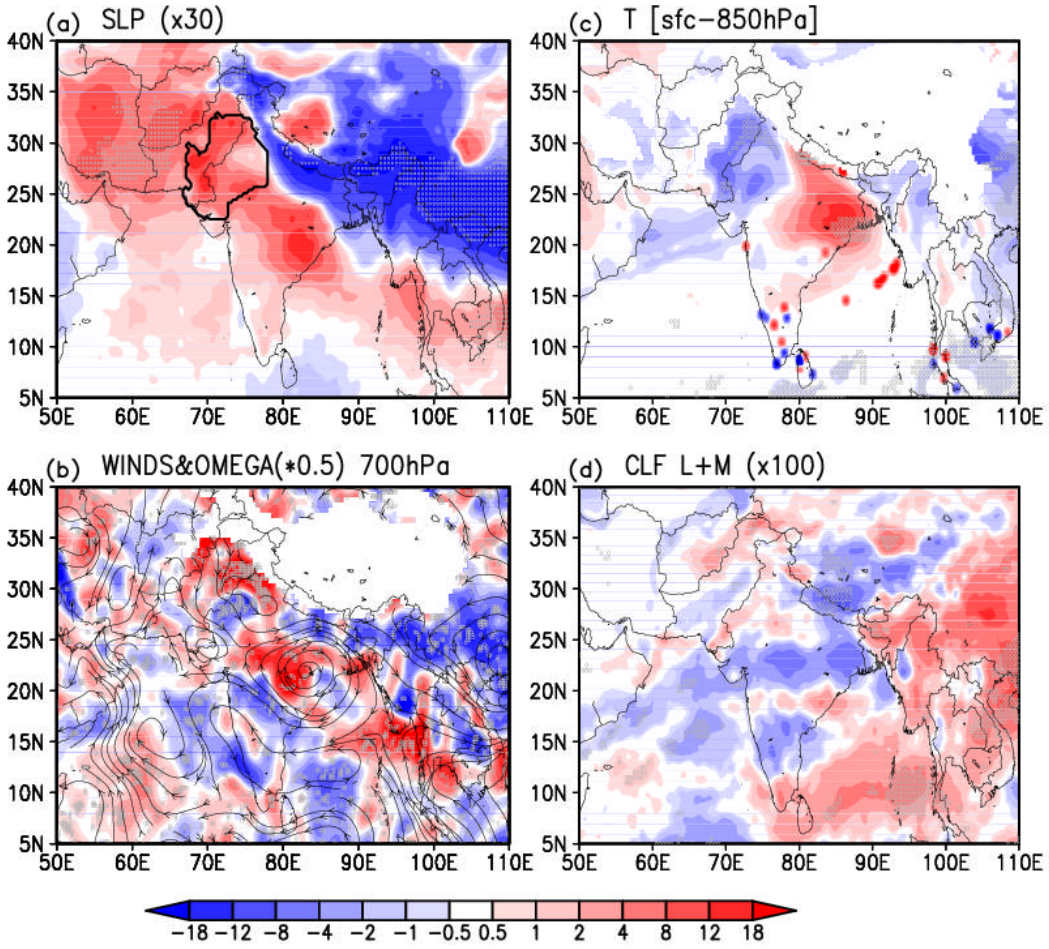

Figure 10: JJA average difference DES-CTL for: (a) sea level pressure (SLP, x30 hPa), (b) 700-hPa horizontal wind (streamlines) and *p*-vertical velocity (x0.5 hPa day^{-1}, positive values upward), (c) temperature vertically averaged between the surface and 850 hPa (°C), and (d) average low and middle cloud fraction (%). The light grey hatching is for statistically significant areas at the 90% confidence level. The black contour in (a) denotes the area of the expanded desert in DES.

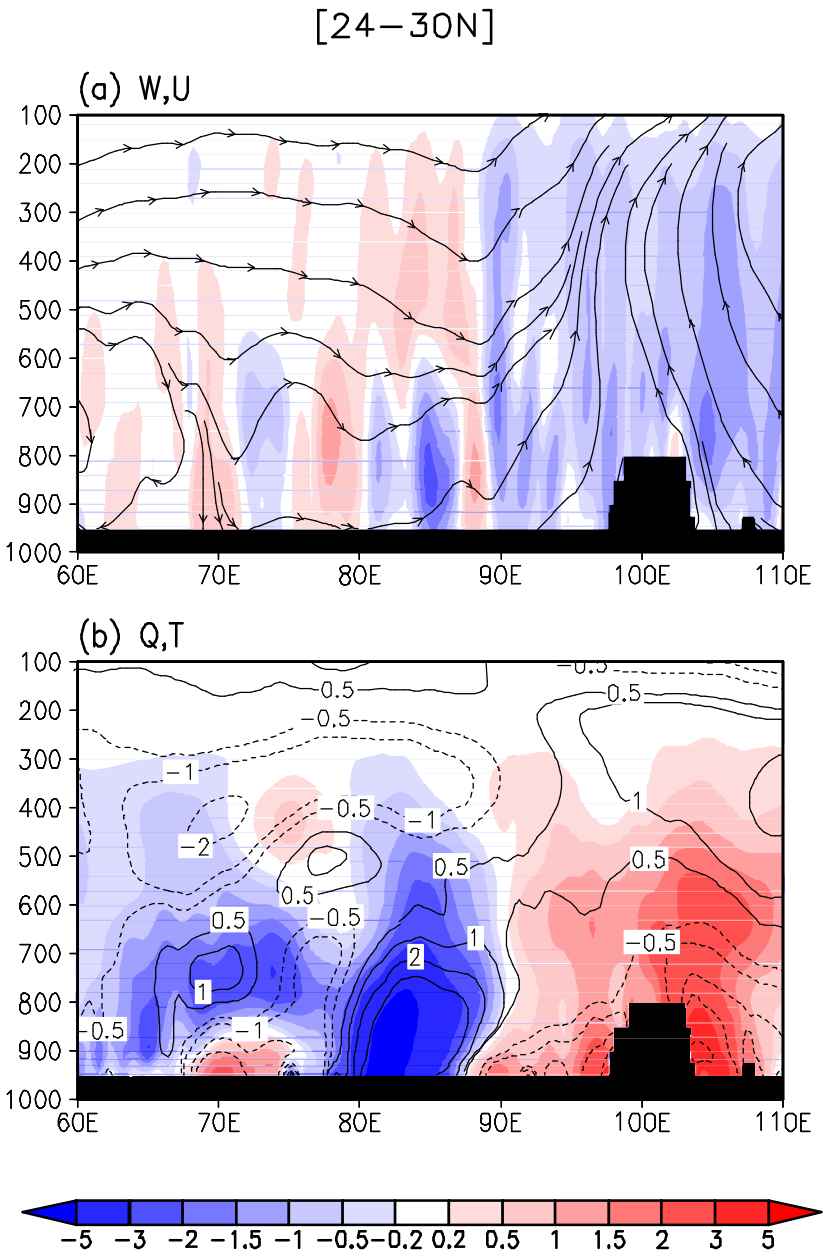

Figure 11: JJA average vertical/zonal cross section averaged between 24°-30°N of the difference DES-CTL for: (a) *p*-vertical velocity (shaded, x0.1 hPa day^{-1}, positive values downward) and zonal circulation (streamlines), and (b) specific humidity (shaded, x10 g kg^{-1}) and temperature (contours, x10°C). Values below orography (black area) have been masked out before averaging.

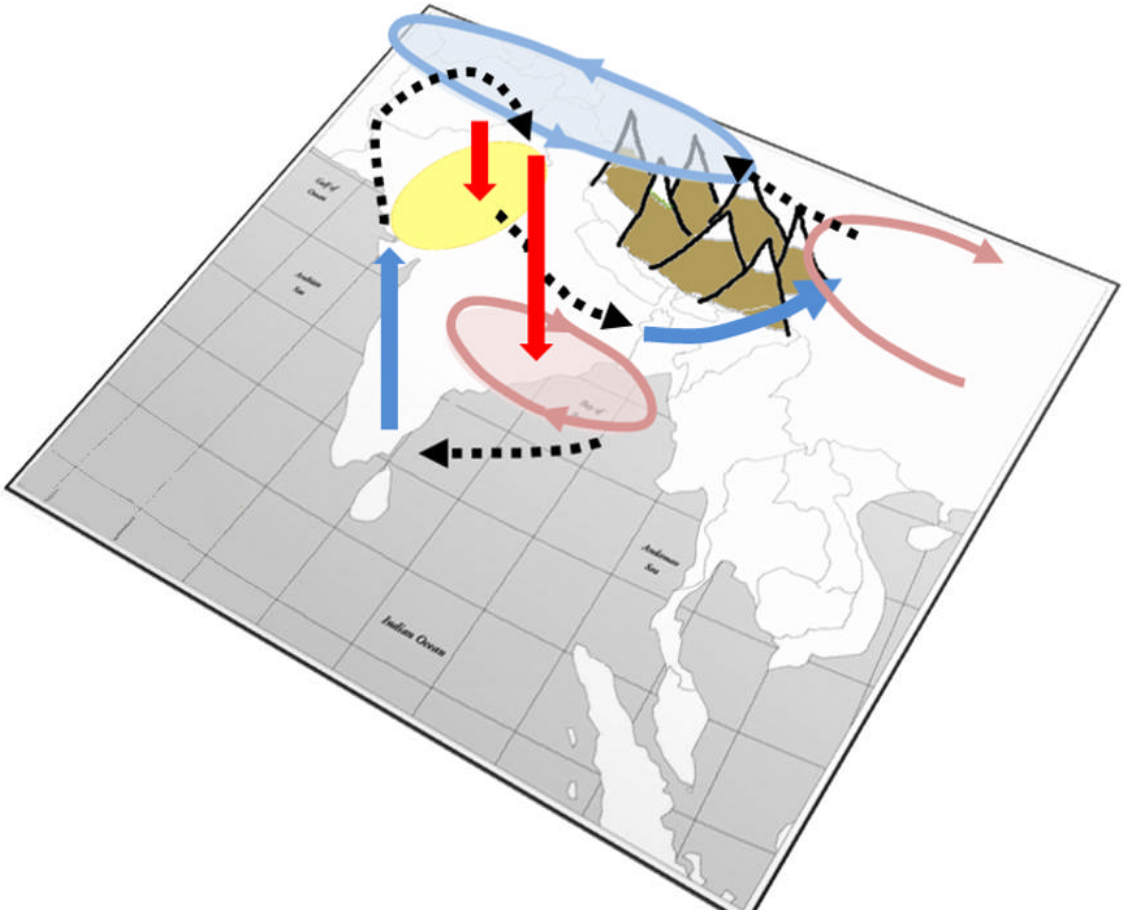

Figure 12: A schematic picture of the JJA average circulation anomalies (i.e., difference DES-CTL) over the Indian subcontinent induced by the expanded desert. The expanded desert is represented by the yellow area. The Himalayas and Tibetan Plateau are also drawn. Color circular areas represent high (red) and low (blue) pressure. Large-scale vertical motion is indicated by red (subsidence) and blue (ascent) thick arrows. Black dotted arrows represent approximately horizontal winds (i.e., mainly associated with horizontal transport).